Journal of Materials Chemistry C

ROYAL SOCIETY OF CHEMISTRY

PAPER

View Article Online
View Journal

Cite this: DOI: 10.1039/d5tc03978a

Multiplet structure of chromium(III) dopants in wide band gap materials

Ilya Popov, [a] Petros-Panagis Filippatos, [a] Shayantan Chaudhuri, [a] Andrei L. Tchougréeff, [b] Katherine Inzani [a] and Elena Besley *[a]

Received 8th November 2025,
Accepted 23rd December 2025

DOI: 10.1039/d5tc03978a

rsc.li/materials-c

Transition metal doping is commonly used for altering the properties of solid-state materials to suit applications in science and technology. Partially filled d-shells of transition metal atoms lead to electronic states with diverse spatial and spin symmetries. Chromium(III) cations have shown great potential for designing laser materials and, more recently, for developing spin qubits in quantum applications. They also represent an intriguing class of chemical systems with strongly correlated multi-reference excited states, due to the d^3 electron configuration. These states are difficult to describe accurately using single-reference quantum chemical methods such as density functional theory (DFT), the most commonly used method to study the electronic structures of solid-state systems. Recently, the periodic effective Hamiltonian of crystal field (pEHCF) method has been shown to overcome some limitations arising in the calculations of excited d-states. In this work, we assess the suitability of DFT and pEHCF to calculate the electronic structure and d–d excitations of chromium(III) dopants in wide band gap host materials. The results will aid computational development of novel transition metal-doped materials and provide a deeper understanding of the complex nature of transition metal dopants in solids.

1 Introduction

Solid-state materials containing transition metal dopants are widely used in many areas of science and engineering, including optoelectronics,[1,2] optics,[3,4] laser technologies,[5–7] photovoltaics and photoelectrochemistry,[8,9] spintronics,[10] semiconductors,[10–12] and quantum computing.[13,14] The distinct properties of transition metal atoms primarily stem from the partially filled d-shells, which lead to a rich multiplet structure of the electronic spectrum, including states with different spatial and spin symmetries and respective degrees of degeneracy. The structure of d-multiplets can be fine-tuned by targeting doping sites with particular symmetries and modifying the host material to affect dopant–host interactions. Chromium(III) (Cr^{3+}) is an attractive dopant choice as its d^3 electronic configuration and corresponding multiplet structure make it a useful candidate for laser materials[15,16] and spin qubits.[13] For example, Sewani *et al.*[13] demonstrated optical initialization and read-out, along with long relaxation times, for the $S = 3/2$ spin population associated with Cr^{3+} dopants in Al_2O_3, where S is the spin quantum number. Continued investigations of Cr^{3+} and other transition metal dopants in different host materials will prove fruitful for quantum technologies by providing a rich set of systems for extended applications.

Dopants with open d-shells exhibit electronic correlation effects[17] of both static and dynamical nature, which occur due to the strong electron–electron interactions characteristic of d-electrons. Static correlations appear when the ground state (or an excited state of interest) exhibits a multi-reference character, *i.e.* it cannot be represented quantitatively by a single Slater determinant (see Benavides-Riveros *et al.*[18] and references therein for further details). Such correlation effects are present in systems with electron (quasi-)degeneracy, which are typical for the d-states of transition metals in highly symmetrical crystal fields,[19] either ideal or slightly distorted. These strongly correlated materials pose a significant challenge to computational research[20,21] as the electronic structure of d-multiplets cannot be adequately captured by standard density functional theory[22,23] (DFT) methods, which are commonly employed to investigate the electronic structures of solid-state systems. Limitations of DFT are most pronounced when calculating the d–d excitations and band gaps of strongly-correlated systems. Advanced methods based on hybrid density-functional approximations can yield better results than standard semi-local functionals,[24] however these solutions are not universal and have limitations on the types of excitations that can be accurately predicted.[25]

This highlights the pressing requirement to search beyond DFT for more reliable methods for electronic structure calculations.

[a] School of Chemistry, University of Nottingham, Nottingham NG7 2RD, UK. E-mail: Elena.Besley@nottingham.ac.uk
[b] Frumkin Institute of Physical Chemistry and Electrochemistry of the Russian Academy of Sciences, Moscow 119071, Russia

One of the most direct ways for addressing strong correlations involves the use of post-Hartree–Fock approaches, such as complete active space self-consistent field (CASSCF),[26] second-order Møller–Plesset perturbation theory[27] and coupled cluster methods.[28] While examples of applying post-Hartree–Fock treatment to solid-state materials exist in the literature,[29–31] the range of applications is limited due to a strong scaling with system size. CASSCF has occasionally been used to calculate the energies of local d–d excitations in small (finite) clusters that represent the first coordination sphere of a transition metal atom in a crystalline system.[14] This approach is, however, associated with significant underestimation of the delocalization effects taking place in extended systems. An alternative to post-Hartree–Fock approaches is to combine multiple electronic structure methods within a hybrid embedding approach, whereby the electronic structure of localized d-shells is treated using a correlated method and the host is described within a weakly correlated (*e.g.* one-electron self-consistent field) treatment. Such a hybrid approach allows one to reduce computational costs while providing a multi-reference description of strongly correlated d-electrons. One of the examples of hybrid electronic structure methods used in solid state theory is dynamical mean-field theory.[32]

In our previous work[33] we extended a hybrid embedding method, called the effective Hamiltonian of crystal field (EHCF),[34,35] to periodic systems (pEHCF). pEHCF has been shown to be successful in describing the d-multiplet structure of various solid materials including oxides,[33] carbodiimides and metal–organic frameworks.[36,37] In this work, we evaluate and compare the suitability of DFT and pEHCF to investigate the electronic structure and d–d excitations of Cr^{3+} dopants in three wide band gap host materials: corundum (α-Al_2O_3), aluminium oxonitridoborate (AlB_4O_6N)[38] and chrysoberyl ($BeAl_2O_4$).

α-Al_2O_3 with Cr^{3+} dopants is a well-known laser material[15,39] with excellent optical properties and distinctive fluorescence which has been also explored for quantum applications.[13] AlB_4O_6N recently synthesized by Widmann *et al.*[38] possesses interesting fluorescence and luminescence properties as well as high thermal stability. Finally, $BeAl_2O_4$ has been widely utilized in solid-state laser technologies due to its exceptional emission properties in the 700–800 nm range.[40] All three host materials show characteristics that are promising for quantum technologies which will benefit from deeper understanding of the complex electronic structure of transition metal dopants in solids provided in this study.

2 Methodology

2.1 Periodic effective hamiltonian of crystal field

The periodic effective Hamiltonian of crystal field (pEHCF) method splits the electronic system into two subsystems, where one contains only the local d-shell(s) of transition metal atoms and the other includes the crystalline environment embedding these shells.[33] The idea of such division of the electronic system into subsystems was first proposed by Harrison,[41] who considered the electronic structure of transition metal oxides as delocalized s,p-bands augmented with local d-multiplets. Mathematically, this splitting is performed by separating a space of one-electron states into d- and l-subspaces spanned by local atomic d- and s,p-orbitals, respectively. Transition metal s,p-orbitals are included in the l-subsystems along with the orbitals of light elements. The many-electron wavefunction of the system is expressed using eqn (1):

$$\Psi = \Psi_{\mathrm{d}}(n_{\mathrm{d}}) \wedge \Psi_{\mathrm{l}}(N - n_{\mathrm{d}}) \tag{1}$$

where Ψ_{d} and Ψ_{l} are the many-electron wavefunctions built in the d- and l-subspaces, respectively, n_{d} is the number of electrons in the d-subspace, N is the total number of electrons in the system, and $\wedge$ stands for the antisymmetric product. The wavefunctions Ψ_{d} and Ψ_{l} are treated differently. In the case of an impurity ion, its strongly correlated d-shell is described by a full configuration interaction wavefunction:

$$\Psi_{\mathrm{d}}(n_{\mathrm{d}}) = \sum_i c_i \Psi_i(n_{\mathrm{d}}) \tag{2}$$

where the summation goes over all configurations, Ψ_i, with coefficients c_i, built on d-orbitals of the impurity ion. This accounts for correlations in the d-shell and accurately reproduces both the energy and spin multiplicity of the excited d-multiplets. The non-correlated l-subsystem is treated using the Hartree–Fock method with the single-determinant wavefunction in the basis of the Bloch states constructed from the s,p-atomic orbitals of the system.[33]

The wavefunction in eqn (1) assumes the number of electrons in both d- and l-subsystems to be fixed and therefore excludes charge transfer states. The presence of such states is taken into account in pEHCF by the Löwdin partitioning technique,[42] which provides effective corrections to the Hamiltonian operators of the subsystems arising due to the electron hopping between them.[33,34] This results in the effective Hamiltonian for the d-subsystem, $\mathcal{H}_{\mathrm{d}}^{\mathrm{eff}}$, having the following form:

$$\begin{aligned}\mathcal{H}_{\mathrm{d}}^{\mathrm{eff}} &= \sum_{\mu\nu}\sum_{\sigma}\left(\mathcal{H}_{\mu\nu}^{\mathrm{d}} + \mathcal{H}_{\mu\nu}^{\mathrm{coul}} + \mathcal{H}_{\mu\nu}^{\mathrm{res}}\right)\mathrm{d}_{\mu\sigma}^{+}\mathrm{d}_{\nu\sigma} \\ &\quad + \frac{1}{2}\sum_{\mu\nu\lambda\eta}\sum_{\sigma\tau}(\mu\nu|\lambda\eta)\mathrm{d}_{\mu\sigma}^{+}\mathrm{d}_{\lambda\tau}^{+}\mathrm{d}_{\eta\tau}\mathrm{d}_{\nu\sigma} + \mathrm{h.c.}\end{aligned} \tag{3}$$

where $\mathrm{d}_{\mu\sigma}^{+}$ and $\mathrm{d}_{\mu\sigma}$ are the electron creation and annihilation operators, respectively, for the μ-th d-orbital, σ and τ correspond to the spin projection, and h.c. is the Hermitian conjugate. The second term includes two-electron one-center integrals $(\mu\nu|\lambda\eta)$ over atomic d-orbitals and describes the two-electron Coulomb interactions within the d-shell. The one-electron part of $\mathcal{H}_{\mathrm{d}}^{\mathrm{eff}}$ includes the bare Hamiltonian of the d-subsystem $(\mathcal{H}^{\mathrm{d}})$, and both Coulomb $(\mathcal{H}^{\mathrm{coul}})$ and resonance $(\mathcal{H}^{\mathrm{res}})$ interactions of d-electrons with electrons and nuclei in the l-subsystem. Contributions from $\mathcal{H}^{\mathrm{coul}}$ and $\mathcal{H}^{\mathrm{res}}$ determine the 'splitting parameter' of the d-orbitals, as referred to within the crystal field theory. In pEHCF, unlike in the crystal field theory, the main contribution to the splitting of d-orbitals is the resonance interactions[33,34] corresponding to the one-electron

transfers between the d- and l-subsystems. Therefore, $\mathcal{H}^{\mathrm{res}}$ is the most important factor when analyzing variations in the splitting parameters during spin-crossover processes. The matrix elements of $\mathcal{H}^{\mathrm{res}}$ have the following form:[33,43]

$$\mathcal{H}^{\mathrm{res}}_{\mu\nu} = \sum_{a,b} \beta_{\mu a}\beta_{\nu b}\left(\Re G^{+}_{ab}(-I_{\mathrm{d}}) + \Re G^{-}_{ab}(-A_{\mathrm{d}})\right) \quad (4)$$

where the summation is over atomic orbitals (AOs) a and b of the l-subsystem, $\beta_{\mu a}$ are resonance (hopping) integrals between the μ-th d-orbital and l-AO a, and I_{d} and A_{d} are the ionization potential and electron affinity, respectively, of the d-subsystem. The orbital-projected Green's functions, $G^{\pm}_{ab}$, of the l-subsystem are expressed as:

$$G^{+}_{ab}(\varepsilon) = \lim_{\delta\to 0^{+}} \sum_{n,\mathbf{k}} (1 - f_{n\mathbf{k}}) \frac{\langle a|n\mathbf{k}\rangle\langle n\mathbf{k}|b\rangle}{\varepsilon - \varepsilon_{n\mathbf{k}} + i\delta} \quad (5)$$

$$G^{-}_{ab}(\varepsilon) = \lim_{\delta\to 0^{+}} \sum_{n,\mathbf{k}} f_{n\mathbf{k}} \frac{\langle a|n\mathbf{k}\rangle\langle n\mathbf{k}|b\rangle}{\varepsilon - \varepsilon_{n\mathbf{k}} + i\delta} \quad (6)$$

In eqn (5) and (6), $\mathbf{k}$ is a vector in the first Brillouin zone, n enumerates bands of the l-subsystem, and $\varepsilon_{n\mathbf{k}}$ and $f_{n\mathbf{k}}$ are energies and occupation numbers, respectively, of the l-bands. Spin variables are omitted for clarity. As can be seen, the resonance term (and therefore the splitting of the d-orbitals) depends on three main factors: the geometry of the first coordination sphere through the resonance integrals between local atomic orbitals ($\beta_{\mu a}$), the occupations of local atomic orbitals forming the first coordination sphere, and the energy difference between d-states and the valence/conduction bands of the l-subsystem.

Solving the linear Schrödinger equation for the wavefunction of the d-system, as shown in eqn (2), with the effective Hamiltonian in eqn (3) produces the whole spectrum of energies for the d-multiplets with all allowed spins and symmetries, among them the ground state. pEHCF electronic structure calculations were performed for geometries obtained by DFT with use of the r^{2}SCAN[44] meta-generalized gradient approximation as described below.

2.2 Density functional theory calculations

Kohn–Sham DFT[22,23] calculations were performed using version 6.4.1 of the Vienna *ab initio* Simulation Package (VASP)[45–47] software within the spin-polarized framework, with the Be ($s^{1.99}p^{0.01}$), B ($2s^2 2p^1$), and O ($2s^2 2p^4$), Al ($3s^2 3p^1$), and Cr_sv ($3s^2 3p^6 3d^5 4s^1$) projector-augmented wave pseudopotentials.[46,48] The r^{2}SCAN[44] meta-generalized gradient approximation (meta-GGA) and the HSE06[49,50] range-separated hybrid generalized gradient approximation were used to perform geometry optimization of the structures and their corresponding density of states. Converged plane-wave cut-off energies of 700 eV, 700 eV, and 750 eV were used for the Al_2O_3, $BeAl_2O_4$, and AlB_4O_6N hosts, respectively. Furthermore, a reciprocal space grid (k-grid) of size 4 × 4 × 2 was used for the primitive unit cells. Convergence tests for the plane-wave cut-off energy and k-point mesh were performed until the total energies from single-point calculations were converged to within 1 meV atom^{-1}. All undoped structures were optimized until the residual forces on all ions were less than 0.001 eV Å^{-1} while for the defected supercells the convergence criterion of forces on all ions was set to 0.01 eV Å^{-1}. The energy convergence criterion for geometry optimizations was set to 10^{-6} eV. For the defect structures, 2 × 2 × 1 expanded supercells of 120, 168, and 192 atoms were used for α-Al_2O_3, $BeAl_2O_4$, and AlB_4O_6N, respectively, to reduce interactions between periodic images of the defects. Delta self-consistent field (ΔSCF) calculations were performed to determine the electronic excited states and the corresponding absorption energies.[51,52] This method is known to be highly effective for calculating excitation energies in quantum defects.[53] The ΔSCF occupation for the spin-up and spin-down components at each k-point was manually set to fix the electron configuration of the system. This provides the total energy of the excited structure without relaxing the geometry. We use this method to simulate the vertical excitations of the first and second excited states of crystal hosts.

3 Results and discussion

The crystal lattices of α-Al_2O_3, AlB_4O_6N, and $BeAl_2O_4$ correspond to trigonal, hexagonal and orthorhombic systems with space groups $R\bar{3}c$,[54] $P6_3mc$[38] and $Pbnm$,[55] respectively. Their experimental crystal parameters along with the values calculated by r^{2}SCAN and HSE06 are collected in Table 1. The calculated values are within 1% of the reported experimental data for all three structures. In all materials, the Cr^{3+} dopant substitutes an aluminium cation (Al^{3+}), leading to the formation of six-coordinate dopant sites of various symmetries, as shown in Fig. 1. The geometries of the Cr^{3+} dopant in each host, obtained with use of r^{2}SCAN and HSE06, are illustrated in Fig. 2 (all structures are given in SI). The dopant site in AlB_4O_6N is of high O_{h} symmetry with minimal distortion from the perfect octahedral coordination characterized by bond length deviation not exceeding 0.01 Å and bond angles deviating from the perfect 90° by 0.8°. α-Al_2O_3 also has a single dopant site that exhibits C_3 symmetry and $BeAl_2O_4$ has two dopant sites characterized by C_{s} (Wyckoff position 4c) and C_i (Wyckoff

Table 1 Experimental (Exp.) lattice parameters (in Å) of α-Al_2O_3, AlB_4O_6N, and $BeAl_2O_4$ compared to the DFT calculations performed in this work

	α-Al_2O_3			AlB_4O_6N			$BeAl_2O_4$		
	Exp.[56]	r^{2}SCAN	HSE06	Exp.[38]	r^{2}SCAN	HSE06	Exp.[55]	r^{2}SCAN	HSE06
a	4.76	4.76	4.75	5.03	5.03	5.02	9.42	9.40	9.39
b	—	—	—	—	—	—	5.48	5.47	5.47
c	12.98	12.98	12.96	8.23	8.23	8.22	4.43	4.42	4.41

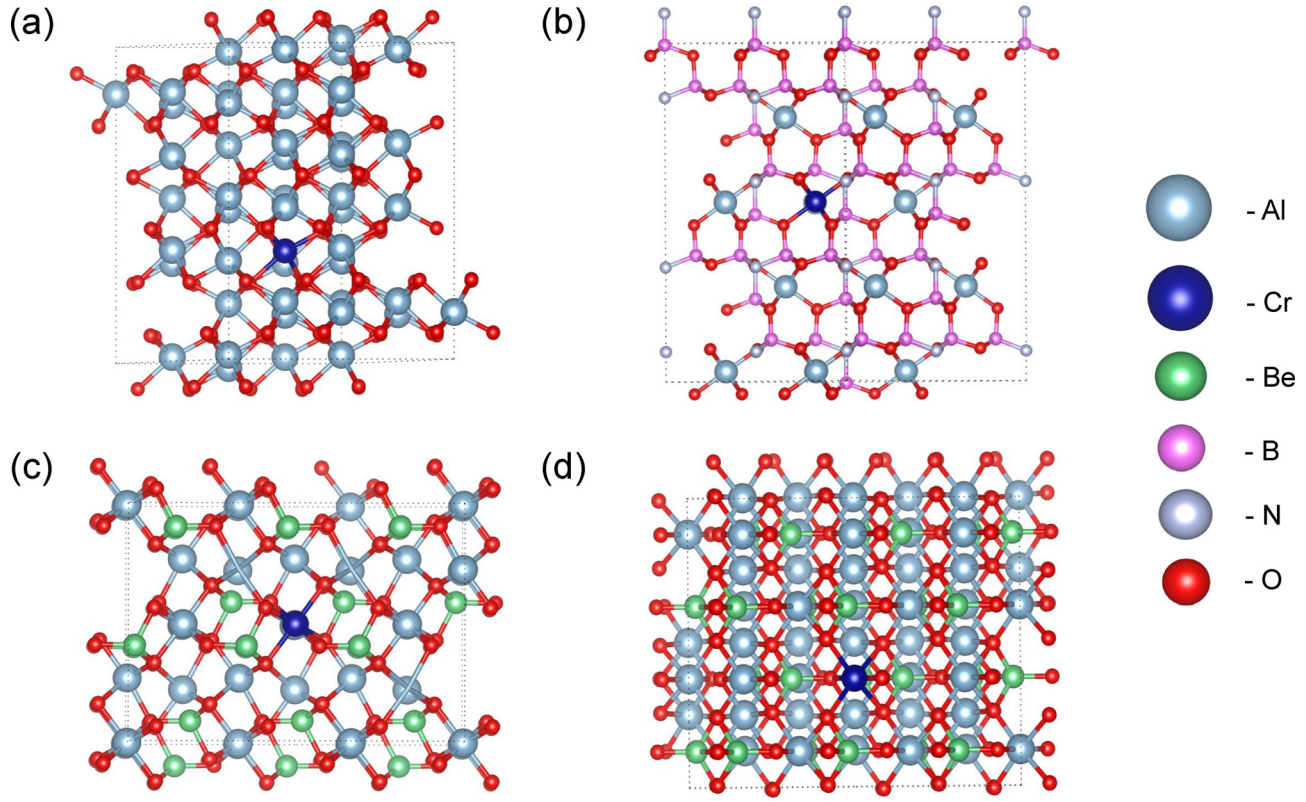

Fig. 1 Crystalline structures of Cr^{3+}-doped (a) α-Al_2O_3, (b) AlB_4O_6N, and $BeAl_2O_4$ at (c) C_s- and (d) C_i-symmetrized sites. Cell boundaries are shown with black dotted lines. All shown crystalline structures are available in SI for both r^{2}SCAN and HSE06 functionals.

position 4*a*) local symmetry point groups. In all cases, the geometries of the coordination spheres are close to that of a regular octahedron, with fairly small distortions resulting in symmetry lowering. In Cr_{Al}^{3+}:α-Al_2O_3, the distortion is characterized by a maximum deviation of 0.05 Å in Cr–O bond lengths and a maximum deviation of 10° in bond angles, whereas in the case of Cr_{Al}^{3+}:$BeAl_2O_4$ these values are 0.09 Å and 10°, respectively. Due to this, we use the notations of irreducible representations of the O_h point group to label electronic states in all three systems and separately discuss splittings of the high-symmetry multiplets caused by the imperfections of dopant sites. As follows from the Tanabe–Sugano diagram of the d^3 configuration in an octahedral field, Cr^{3+} cations must always have a high-spin quartet ($S = 3/2$) ground state ($^4A_2$), and a set of low-spin quartet and doublet ($S = 1/2$) excited states, the order and energies of which depend on the interactions of the Cr^{3+} dopant with its host. Transitions between these states correspond to the class of crystal field d–d excitations and can be experimentally probed *via* ultraviolet-visible and photoluminescence spectroscopy. We further test the capabilities of DFT and pEHCF in reproducing the energies and spin-symmetries of excited d-multiplets of Cr^{3+} dopants.

First, we analyse the one-electron states of the three systems, as calculated using DFT and pEHCF methods. The atomic orbital-projected density of states (DOS) for the ground states of Cr^{3+}-doped α-Al_2O_3, AlB_4O_6N, and $BeAl_2O_4$ are shown in Fig. 3. For all systems, as can be seen from the r^{2}SCAN-calculated DOS, the narrow d-bands of Cr^{3+} lie within the gap between the wide sp valence and conduction bands of the host. The small width of the d-bands indicates a small degree of coupling between the d-shell and sp-states, supporting the assumption regarding the locality of d-shells that is employed within pEHCF. In the case of DFT, there is a minor contribution from the oxygen 2p states in the gap states reflecting a small degree of hybridization with the chromium 3d states. The pEHCF-calculated DOS plots qualitatively agree with DFT regarding the position of the one-electron d-states and the structure of the frontier sp-bands. The valence band of the sp-subsystem mostly comprises oxygen 2p orbitals for each host material, whereas the conduction band has significant contributions from aluminium 3p orbitals. If the concentration of Cr^{3+} dopants is sufficiently low, the gap between the valence and conduction sp-bands should be close to the band gap of the host material.

Our calculations show that for the given unit cells, the sp-band gaps of the doped materials are smaller than the band gaps of the pure hosts by 0.1–0.2 eV, which can be compared against corresponding experimental values. Experimental values of the band gap of α-Al_2O_3 have been reported to range from 8.15–9.40 eV depending on conditions,[57] while the reported experimental value for $BeAl_2O_4$ is 9.00 eV.[58] The calculated values of the band gap are compared to the available experimental data in Table 2. It shows that pEHCF systematically overestimates the gap by 0.50–1.50 eV for Cr_{Al}^{3+}:α-Al_2O_3 and by 2.00 eV for Cr_{Al}^{3+}:$BeAl_2O_4$ as the Hartree–Fock method is

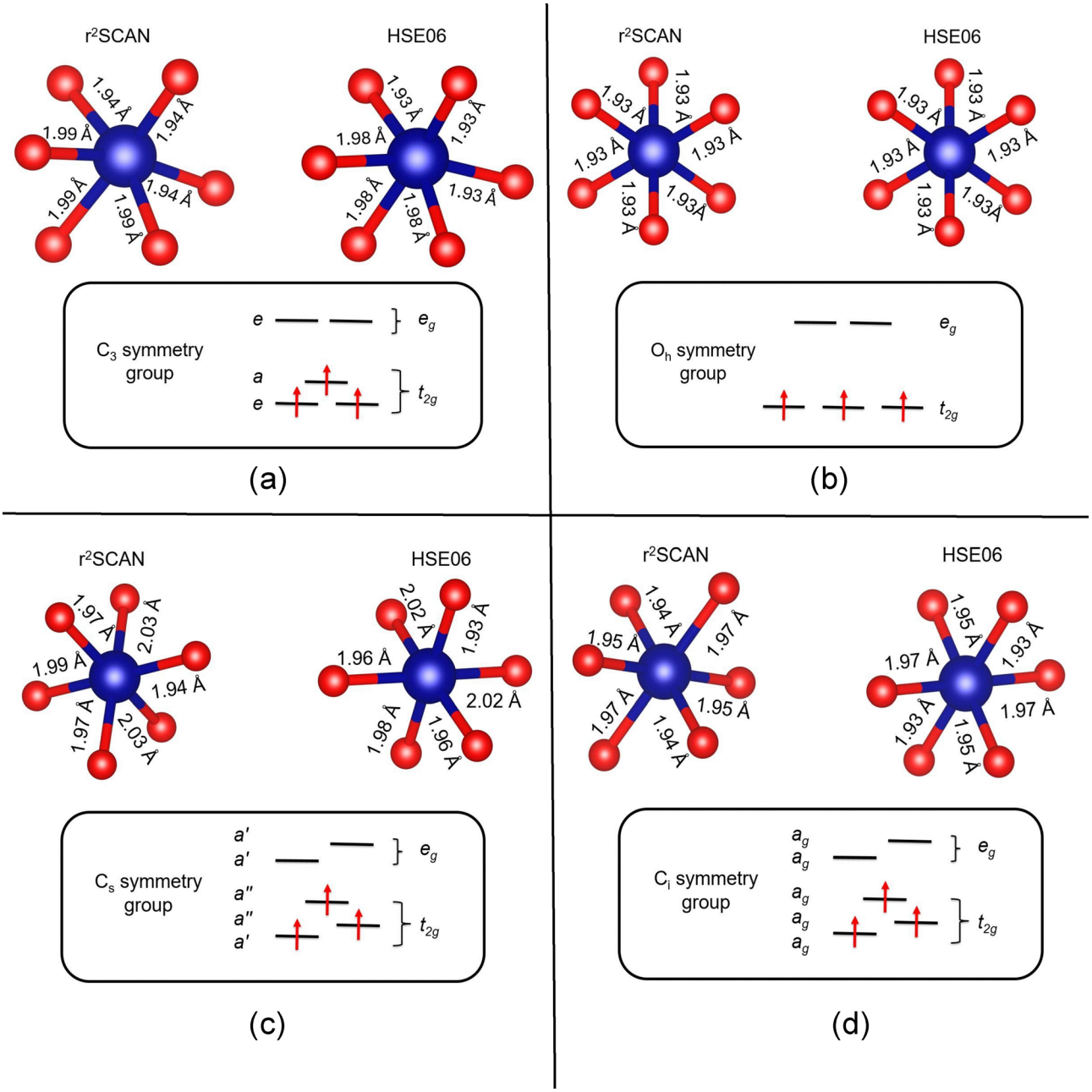

Fig. 2 Ground-state geometries of the Cr coordination sphere and the splitting diagrams of the one-electron d-states for (a) α-Al_2O_3, (b) AlB_4O_6N, and $BeAl_2O_4$ at (c) C_s- and (d) C_i-sites. The corresponding splitting parameters of the one-electron d-states calculated with r^{2}SCAN, HSE06, and pEHCF are presented in Table 2.

used to calculate the electronic structure of the sp-subsystem. In contrast, r^{2}SCAN underestimates the band gap by about 1.5 eV for both materials whilst HSE06 gives the improved values of 8.15 eV for α-Al_2O_3 and 8.38 eV for $BeAl_2O_4$. No experimental band gap value has been reported for AlB_4O_6N, but we calculate a band gap of 9.78 eV using HSE06. Other reported theoretical band gap values range from 7.32–9.31 eV, depending on the computational method.[38]

Splitting diagrams for the one-electron d-states and the ground state, as calculated with pEHCF, r^{2}SCAN and HSE06, are shown in Fig. 2. All methods qualitatively follow the same symmetry considerations, exhibiting a significant t_{2g}–e_g splitting characteristic of an octahedral crystal field. An additional minor splitting within the threefold degenerate t_{2g} manifold is present in Cr_{Al}^{3+}:α-Al_2O_3 (C_3 symmetry), while full degeneracy lifting occurs for Cr_{Al}^{3+}:$BeAl_2O_4$, which possesses lower-symmetry (C_s and C_i) dopant sites. Quantitatively, the absolute magnitudes of crystal-field splittings differ significantly between pEHCF and the DFT methods (Table 2). For instance, the r^{2}SCAN splitting of t_{2g}–e_g has values of around 4.00–4.40 eV; HSE06 provides splittings of 6.10–6.60 eV, while pEHCF shows splittings of 2.08–3.47 eV. This disparity is to be expected due to

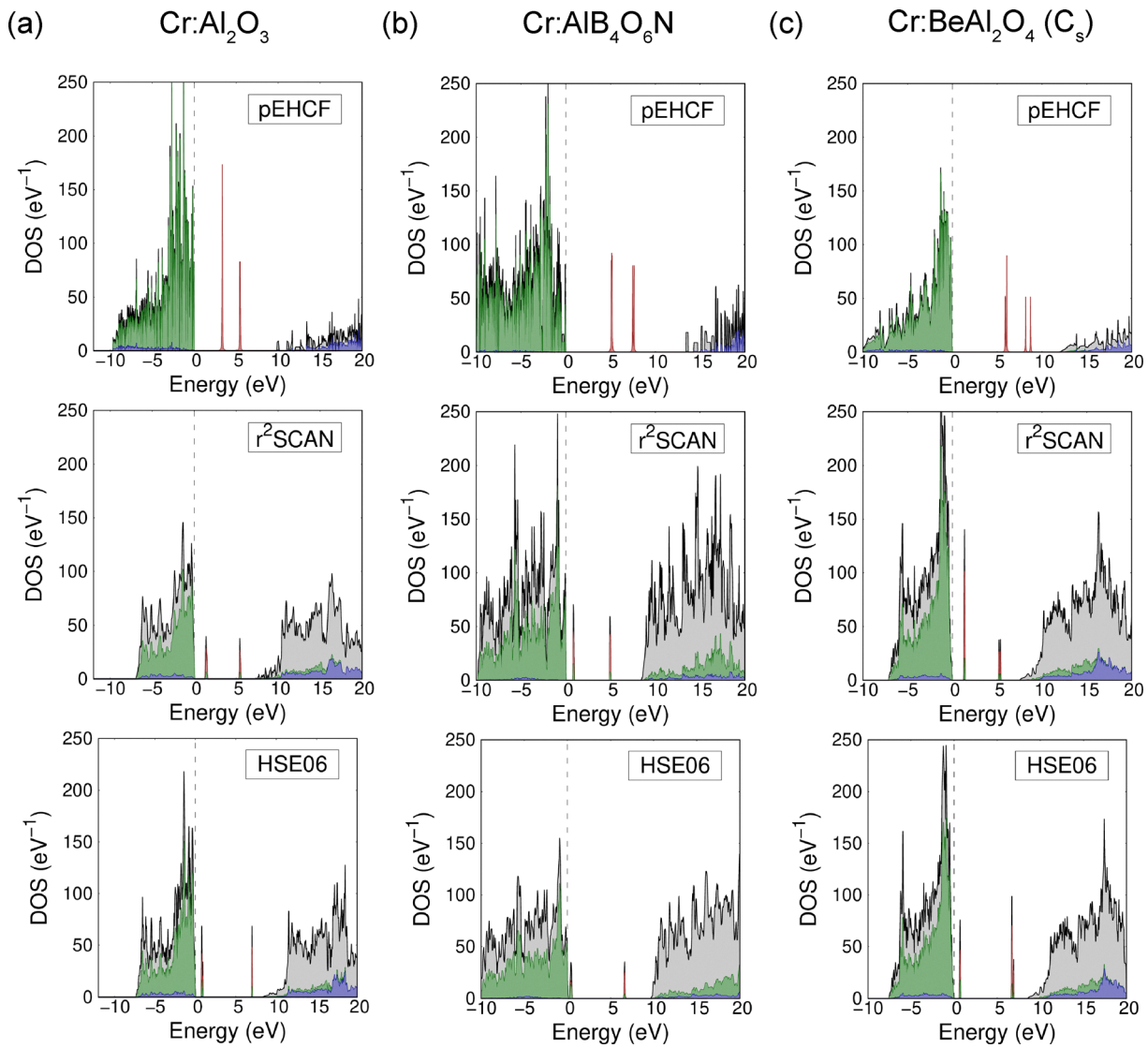

Fig. 3 The atomic orbital-projected density of states (DOS) for Cr^{3+}-doped (a) α-Al_2O_3, (b) AlB_4O_6N and (c) $BeAl_2O_4$ (C_s), as calculated using the r^{2}SCAN, HSE06 and pEHCF. The total density of states, chromium 3d, oxygen 2p and aluminium 3p states are shown in gray, red, green and blue, respectively. Other atomic orbitals are not shown for clarity. For the purpose of comparison across all three methods, the position of the reference point on the energy axis is chosen such that the top of the sp-valence band corresponds to 0 eV. In pEHCF, the peaks corresponding to the d-states indicate the position of the one-electron d-orbitals. This representation does not fully reflect the complexity of the electronic structure of the d-system containing multi-reference many-electron multiplets described by pEHCF.

Table 2 Energies of the one-electron d-states of Cr^{3+} dopants and sp-band gaps calculated using different quantum mechanical methods. The calculated values of the band gap are compared to available experimental data for α-Al_2O_3 and $BeAl_2O_4$

	α-Al_2O_3			AlB_4O_6N			$BeAl_2O_4$ (C_s)			$BeAl_2O_4$ (C_i)		
Host →	pEHCF	r^{2}SCAN	HSE06	pEHCF	r^{2}SCAN	HSE06	pEHCF	r^{2}SCAN	HSE06	pEHCF	r^{2}SCAN	HSE06
t_{2g} [eV]	0.00	0.00	0.00	0.00	0.00	0.00	0.00	0.00	0.00	0.00	0.00	0.00
	0.00	0.00	0.00	0.06	0.05	0.11	0.19	0.05	0.05	0.14	0.09	0.08
	0.03	0.10	0.10	0.10	0.05	0.11	0.30	0.07	0.09	0.37	0.19	0.15
e_g [eV]	2.08	4.04	6.21	2.40	4.15	6.32	2.50	3.92	6.11	2.95	4.29	6.47
	2.15	4.04	6.21	2.55	4.15	6.32	2.69	4.06	6.26	3.17	4.40	6.59
E_{gap}^{sp} [eV]	9.86	7.22	8.21	13.45	7.99	9.72	11.71	7.45	8.45	11.77	7.45	8.42
Exp. E_{gap}^{sp} [eV]		8.15–9.40[57]			—			9.00[58]			9.00[58]	

the nature of the one-electron energies in both methods. pEHCF splitting diagrams correspond to the eigenvalues of the one-electron part of the effective Hamiltonian, whereas energy levels produced by DFT already include an effect of

d–d electron interactions. From this point of view, pEHCF produces splitting parameters that are usually discussed in the literature related to spectroscopy of transition metal ions, such as $10Dq$ in the O_h crystal field.

Many-electron multiplet energies calculated using r^{2}SCAN, HSE06, and pEHCF are detailed in Tables 3–5 for the three materials, where they are compared against experimental values. Theoretically, the simplest transition is $^4A_2 \rightarrow {}^4T_2$, which corresponds to the promotion of one electron from the t_{2g}-orbital to the e_g-orbital. Both multiplets can be accurately described using a single determinant wavefunction;[19] the effect of static correlations should therefore be minor. r^{2}SCAN and HSE06 accurately reproduce the energy of this transition for all materials with absolute errors compared to experiment ranging between 0.10–0.15 eV, and pEHCF also provides the same level of accuracy. As shown in Table 3, CASSCF calculations previously performed[14] for a finite $[CrO_6]^{9-}$ cluster cut out from Cr^{3+}:Al_2O_3 give slightly larger errors for the $^4A_2 \rightarrow {}^4T_2$ transition as compared to DFT and pEHCF.

Other excited states, such as ^2E, have significant multi-reference character, and correct description of their electronic structure is therefore much more challenging for DFT. As has been previously shown with ΔSCF, the low-spin excited states may not be achievable or could be significantly underestimated with respect to experimental values.[59] This is clearly illustrated by the results for the ^2E multiplet that presents an interest for Cr^{3+}-based spin qubits as it plays an important role in the inter-system crossing pathway.[59] Both r^{2}SCAN and HSE06 consistently underestimate the energy of the ^2E state as compared to experiments, with absolute errors ranging between 0.50–0.60 eV. At the same time, pEHCF provides good accuracy for the $^4A_2 \rightarrow {}^2E$ lines for all materials, with absolute errors ranging between 0.07–0.11 eV. The $^2T_1$ and $^2T_2$ states are even more complicated, as their energies cannot be calculated using ΔSCF at all due to their multi-reference nature. This is because their many-determinant wavefunctions cannot be approximated by the one-electron population matrix that is used to set up a trial Kohn–Sham wavefunction in ΔSCF. Full configuration interaction treatment of the d-shell, as implemented in pEHCF, permits the $^2T_1$ and $^2T_2$ wavefunctions to be determined and results in energies that are in good agreement with experimental data for all systems.

Regarding the second excited quartet state, $^4T_1$, all methods agree well with experimental data. For Cr_{Al}^{3+}:α-Al_2O_3, pEHCF successfully captures the reported experimental values ranging from 3.01–3.12 eV.[60–62] r^{2}SCAN and HSE06 give excitation energies of 3.31 eV and 3.05 eV, respectively. For Cr_{Al}^{3+}:Al-B_4O_6N, the second excited quartet is calculated to be 3.30 eV in pEHCF and 3.46–3.49 eV by DFT methods, which can be compared to the experimental value of 3.26 eV.[38] Finally, for Cr_{Al}^{3+}:$BeAl_2O_4$, the experimentally reported value of 3.02 eV[63] agrees well with our r^{2}SCAN-calculated energy of 2.98 eV for the C_s-symmetrized site and our HSE06-calculated energy of 3.02 eV for the C_i-symmetrized site. In contrast, pEHCF overestimates the energy of $^4A_2 \rightarrow {}^4T_1$ transition by 0.20 eV and 0.10 eV for the C_s- and C_i-symmetrized sites, respectively.

We also note an interesting discrepancy with experimental data for Cr_{Al}^{3+}:$BeAl_2O_4$ at the C_i dopant site. As shown in Table 5, the pEHCF-, r^{2}SCAN-, and HSE06-calculated energies for the $^4A_2 \rightarrow {}^4T_2$ transition are in good agreement with the experimentally observed line for the C_s dopant site. However, for the C_i dopant site, the $^4A_2 \rightarrow {}^4T_2$ transition is significantly overestimated by all computational methods: by around 0.6–0.9 eV with pEHCF and 0.4 eV with DFT. This indicates that the C_s dopant site might be largely responsible for the experimental emission, whereas the C_i dopant site plays a minor role. This conclusion is further supported by our DFT calculations showing that Cr^{3+} in the C_s-symmetrized site lies lower in energy than the C_i-symmetrized site by 0.17 eV and 0.19 eV for r^{2}SCAN and HSE06, respectively. A wide range of experimental studies confirm the preference of the C_s site. For instance, electron paramagnetic resonance and optical absorption spectroscopic analyses of $BeAl_2O_4$ indicate that 75% of Cr^{3+} ions substitute the C_s-symmetrized site.[64] Using X-ray absorption spectroscopy, Bordage *et al.*[65] also confirmed Cr^{3+} substitution at the C_s-symmetrized site to be 70%. These experimental findings are consistent with our computational results suggesting that the optical features observed experimentally predominantly correspond to Cr^{3+} substitution at the energetically and structurally favoured C_s-symmetrized site.

Our results show that, for the excited multiplets of Cr^{3+}, r^{2}SCAN and HSE06 functionals consistently give close energy values and perform particularly well for the high-spin states. Previous work on NV-like defects has shown that both hybrid density-functional approximation and meta-GGA can yield reliable predictions for the formation energy and charge transition levels.[66] However, as shown in ref. 67, HSE06 may fail for

Table 3 Calculated energies (in eV) of excited d-multiplets of Cr_{Al}^{3+}:α-Al_2O_3 using different quantum mechanical methods compared to optical absorption spectroscopy data and CASSCF calculations for a $[CrO_6]^{9-}$ cluster (cut from Cr_{Al}^{3+}:α-Al_2O_3) from Shang *et al.*[14] The $^4A_2 \rightarrow {}^2E$ transition is extracted from the *R*-line in the experimental references

Transition	Experiment	pEHCF	r^{2}SCAN	HSE06	CASSCF
$^4A_2 \rightarrow {}^2E$	1.78;[60] 1.80[61]	1.90	1.21	1.14	1.78[14]
$^4A_2 \rightarrow {}^2T_1$	Not resolved	1.97; 2.00	—	—	—
$^4A_2 \rightarrow {}^4T_2$	2.22;[60,61] 2.25;[62] 2.28[60]	2.08; 2.14	2.37	2.36	2.49[14]
$^4A_2 \rightarrow {}^2T_2$	Not resolved	2.82; 2.83; 2.90	—	—	—
$^4A_2 \rightarrow {}^4T_1$	3.01–3.03;[60]	2.94; 2.97; 3.11	3.31	3.05	—

Table 4 Calculated energies (in eV) of excited d-multiplets of Cr_{Al}^{3+}:Al-B_4O_6N using different quantum mechanical methods compared to photoluminescence excitation and emission spectroscopy data for the $^4A_2 \rightarrow {}^2E$ transition from Widmann *et al.*[38]

Transition	Experiment	pEHCF	r^{2}SCAN	HSE06
$^4A_2 \rightarrow {}^2E$	1.81	1.91	1.25	1.12
$^4A_2 \rightarrow {}^2T_1$	1.89	1.99; 2.01	—	—
$^4A_2 \rightarrow {}^4T_2$	2.43	2.40; 2.42; 2.44	2.46	2.49
$^4A_2 \rightarrow {}^2T_2$	2.70	2.89; 2.92	—	—
$^4A_2 \rightarrow {}^4T_1$	3.26	3.30; 3.32	3.49	3.46

Table 5 Calculated energies (in eV) of excited d-multiplets of Cr_{Al}^{3+}:$BeAl_2O_4$ using different quantum mechanical methods compared to ultraviolet-visible spectroscopy data from Demirbas *et al.*[63]

		C_s site			C_i site		
Transition	Experiment	pEHCF	r^{2}SCAN	HSE06	pEHCF	r^{2}SCAN	HSE06
$^4A_2 \rightarrow {}^2E$	1.82	1.89; 1.90	1.27	1.17	1.80; 1.89	1.22	1.15
$^4A_2 \rightarrow {}^2T_1$	1.91	1.95; 1.99; 2.00	—	—	1.91; 2.01; 2.04	—	—
$^4A_2 \rightarrow {}^4T_2$	2.10	2.34; 2.41; 2.52	2.18	2.16	2.72; 2.91; 2.95	2.47	2.49
$^4A_2 \rightarrow {}^2T_2$	—	2.91; 2.95; 2.96	—	—	3.00; 3.04; 3.09	—	—
$^4A_2 \rightarrow {}^4T_1$	3.02	3.23; 3.37	2.98	2.72	3.64	3.16	3.02

transition metal containing systems due to the Coulombic interactions between localised d-electrons not being sufficiently screened. This results in an incomplete removal of self-interaction error and violation of the generalized Koopmans' condition. This makes r^{2}SCAN a competitive, lower-cost alternative to hybrid density-functional approximations for systems containing transition metal atoms, particularly when combined with the pEHCF multi-reference treatment of the d-shell.

Conclusions

In this work, we have used the r^{2}SCAN meta-GGA and the range-separated HSE06 hybrid density-functional approximation, alongside the wavefunction-based pEHCF method, to investigate the electronic structure of the low-lying d–d excited states of chromium(III) dopants in three wide band gap materials. Our results demonstrate that the energy of the $^4A_2 \rightarrow {}^4T_2$ and $^4A_2 \rightarrow {}^4T_1$ transitions between single-reference quartet states can be accurately described by all three methods with a similar level of accuracy. r^{2}SCAN and HSE06 yield similar results for the high-spin excited states, making r^{2}SCAN an accurate and relatively low-cost density-functional approximation compared to HSE06. At the same time, high-spin to low-spin transitions are much more difficult to capture with DFT methods. However, as the pEHCF method treats open d-shells at the configuration interaction level, the energies of all the transitions can be calculated at a high level of accuracy. A combination of DFT and pEHCF, therefore, provides a reliable tool for the quantitative study of transition metal-doped materials. While DFT is effective in predicting ground-state geometry and properties and certain high-spin excited states, its underestimation of the energies of low-spin configurations due to their multi-reference nature is a considerable limitation. In contrast, pEHCF, with its full configuration interaction treatment of the d-shell, excels at capturing these multiplets, as well as the energies of spin-forbidden transitions. Our proposed computational framework can guide future materials design for optical, magnetic and quantum technologies.

Author contributions

I. P. – conceptualization, investigation (pEHCF calculations), data curation, visualization, writing – original draft & editing. P.-P. F. – investigation (DFT calculations), data curation, visualization, writing – original draft & editing. S. C. – investigation (DFT calculations), writing – review & editing. A. L. T. – conceptualization, writing – review & editing. K. I. – conceptualization, supervision, writing – review & editing. E. B. – conceptualization, supervision, writing – review & editing, project administration.

Conflicts of interest

There are no conflicts to declare.

Data availability

The structural data supporting this article have been included as part of the supplementary information (SI). Supplementary information is available. See DOI: https://doi.org/10.1039/d5tc03978a.

Acknowledgements

E. B. acknowledges a Royal Society Wolfson Fellowship and the EPSRC Program Grant ''Enabling Net Zero and the AI Revolution with ultra-low energy 2D Materials and Devices (NEED2D)'' [UKRI-1249] for funding. E. B. and I. P. are funded by the EPSRC Program Grant ''Metal Atoms on Surfaces and Interfaces (MASI) for Sustainable Future'' [EP/V000055/1]. K. I. and P.-P. F. are funded by the EPSRC Fellowship Programme [EP/W028131/1] and S. C. is funded by Wellcome Leap as part of the Quantum for Bio Program. The work of A. L. T. is supported by the Ministry of Science and Higher Education of the Russian Federation. Computing resources were provided by the University of Nottingham, the EPSRC-funded HPC Midlands+ consortium [EP/T022108/1] for access to Sulis, and the EPSRC-funded High-End Computing Materials Chemistry Consortium [EP/X035859/1] for access to the ARCHER2 UK National Supercomputing Service (https://www.archer2.ac.uk). P.-P. F. acknowledges Prof. Ádám Gali and Dr Gergő Thiering (Wigner Research Centre for Physics, Hungarian Academy of Sciences) for useful discussions. The authors also thank the reviewers for their valuable assessment of this work.

References

1 Z. Suo, J. Dai, S. Gao and H. Gao, *Results Phys.*, 2020, **17**, 103058.

2 K. O. Egbo, A. E. Adesina, C. V. Ezeh, C. P. Liu and K. M. Yu, *Phys. Rev. Mater.*, 2021, **5**, 094603.
3 K. Greeshma, A. K. Adiyodi, S. Ancy, S. P. Dhale, N. S. Ugemuge and K. Nissamudeen, *Spectrochim. Acta, Part A*, 2025, **337**, 126086.
4 S. Dhale, A. Nande, N. Ugemuge, V. S. Singh and S. V. Moharil, *Spectrochim. Acta, Part A*, 2025, **337**, 126088.
5 I. T. McKinnie, L. A. W. Gloster, Z. X. Jiang and T. A. King, *Appl. Opt.*, 1996, **35**, 4159.
6 T. Carrig, A. Zakel, G. Wagner and W. Alford, 2005 IEEE LEOS Annual Meeting Conference Proceedings, 2005, pp. 260–261.
7 N. Z. Alpaslan Yayli, A. C. Talmac, S. Keskin Tunc, D. Akbal, D. Altindal and A. S. Ertugrul, *Lasers Med. Sci.*, 2021, **37**, 665–674.
8 S. Wieghold, Y. Luo, A. S. Bieber, J. Lackner, N. Shirato, Z. A. VanOrman, D. Rosenmann, K. Nienhaus, B. Lai, G. U. Nienhaus, V. Rose and L. Nienhaus, *Chem. Mater.*, 2021, **33**, 6099–6107.
9 H. Maruska and A. K. Ghosh, *Sol. Energy Mater.*, 1979, **1**, 237–247.
10 V. Dierolf, I. Ferguson and J. Zavada, *Rare Earth and Transition Metal Doping of Semiconductor Materials. Synthesis, Magnetic Properties and Room Temperature Spintronics*, Woodhead Publishing, 2016.
11 Y. Murai, S. Zhang, T. Hotta, Z. Liu, T. Endo, H. Shimizu, Y. Miyata, T. Irisawa, Y. Gao, M. Maruyama, S. Okada, H. Mogi, T. Sato, S. Yoshida, H. Shigekawa, T. Taniguchi, K. Watanabe, R. Canton-Vitoria and R. Kitaura, *ACS Nano*, 2021, **15**, 19225–19232.
12 E. C. R. Lopez, *Next Mater.*, 2025, **8**, 100550.
13 V. K. Sewani, R. J. Stöhr, R. Kolesov, H. H. Vallabhapurapu, T. Simmet, A. Morello and A. Laucht, *Phys. Rev. B*, 2020, **102**, 104114.
14 L. Shang, Q. Chen, W. Jing, C.-G. Ma, C.-K. Duan and J. Du, *Phys. Rev. Mater.*, 2022, **6**, 086201.
15 T. H. Maiman, *Nature*, 1960, **187**, 493–494.
16 A. Sennaroglu and Y. Morova, *Appl. Phys. B:Lasers Opt.*, 2021, **128**, 9.
17 P.-O. Löwdin, *Phys. Rev.*, 1955, **97**, 1509–1520.
18 C. L. Benavides-Riveros, N. N. Lathiotakis and M. A. L. Marques, *Phys. Chem. Chem. Phys.*, 2017, **19**, 12655–12664.
19 Y. Tanabe and S. Sugano, *J. Phys. Soc. Jpn.*, 1954, **9**, 753–766.
20 J. Lischner, J. Deslippe, M. Jain and S. G. Louie, *Phys. Rev. Lett.*, 2012, **109**, 036406.
21 E. Pavarini, *Riv. Nuovo Cimento*, 2021, **44**, 597–640.
22 P. Hohenberg and W. Kohn, *Phys. Rev.*, 1964, **136**, B864–B871.
23 W. Kohn and L. Sham, *Phys. Rev.*, 1965, **140**, A1133–A1138.
24 K. Czelej, M. Rey Lambert, M. E. Turiansky, A. Koshevarnikov, S. Mu and C. G. Van de Walle, *ACS Nano*, 2024, **18**, 28724–28734.
25 J. Yang, S. Falletta and A. Pasquarello, *npj Comput. Mater.*, 2023, **9**, 108.
26 J. Olsen, *Int. J. Quantum Chem.*, 2011, **111**, 3267–3272.
27 M. Head-Gordon, J. A. Pople and M. J. Frisch, *Chem. Phys. Lett.*, 1988, **153**, 503–506.
28 B. Jeziorski and H. J. Monkhorst, *Phys. Rev. A:At., Mol., Opt. Phys.*, 1981, **24**, 1668–1681.
29 G. H. Booth, A. Grüneis, G. Kresse and A. Alavi, *Nature*, 2012, **493**, 365–370.
30 T. Gruber, K. Liao, T. Tsatsoulis, F. Hummel and A. Grüneis, *Phys. Rev. X*, 2018, **8**, 021043.
31 V. A. Neufeld, H.-Z. Ye and T. C. Berkelbach, *J. Phys. Chem. Lett.*, 2022, **13**, 7497–7503.
32 A. Georges, G. Kotliar, W. Krauth and M. J. Rozenberg, *Rev. Mod. Phys.*, 1996, **68**, 13–125.
33 I. Popov, E. Plekhanov, A. Tchougréeff and E. Besley, *Mol. Phys.*, 2023, **121**, e2106905.
34 A. V. Soudackov, A. L. Tchougréeff and I. A. Misurkin, *Theor. Chim. Acta*, 1992, **83**, 389–416.
35 A. L. Tchougréeff, A. V. Soudackov, J. van Leusen, P. Kögerler, K. Becker and R. Dronskowski, *Int. J. Quantum Chem.*, 2015, **116**, 282–294.
36 I. Popov, D. Raenko, A. Tchougréeff and E. Besley, *J. Phys. Chem. C*, 2023, **127**, 21749–21757.
37 I. Popov, A. Tchougréeff and E. Besley, *J. Chem. Phys.*, 2025, **163**, 054117.
38 I. Widmann, G. Kinik, M. Jähnig, R. Glaum, M. Schwarz, C. Wüstefeld, D. Johrendt, M. Tribus, C. Hejny, L. Bayarjargal, L. Dubrovinsky, G. Heymann, M. Suta and H. Huppertz, *Adv. Funct. Mater.*, 2024, **34**, 2400054.
39 B. Ratzker, A. Wagner, B. Favelukis, S. Goldring, S. Kalabukhov and N. Frage, *J. Eur. Ceram. Soc.*, 2021, **41**, 3520–3526.
40 R. M. F. Scalvi, M. S. Li and L. V. Scalvi, *Phys. Chem. Miner.*, 2005, **31**, 733–737.
41 W. Harrison, *Electronic Structures and the Properties of Solids: The Physics of the Chemical Bond*, Freeman Co, San Francisco, 1980.
42 P. Löwdin, *Int. J. Quantum Chem.*, 1982, **21**, 69–92.
43 A. Tokmachev and A. Tchougréeff, *J. Solid State Chem.*, 2003, **176**, 633–645.
44 J. W. Furness, A. D. Kaplan, J. Ning, J. P. Perdew and J. Sun, *J. Phys. Chem. Lett.*, 2020, **11**, 8208–8215.
45 G. Kresse and J. Furthmüller, *Phys. Rev. B:Condens. Matter Mater. Phys.*, 1996, **54**, 11169.
46 G. Kresse and D. Joubert, *Phys. Rev. B:Condens. Matter Mater. Phys.*, 1999, **59**, 1758.
47 G. Kresse and J. Furthmüller, *Comput. Mater. Sci.*, 1996, **6**, 15–50.
48 P. E. Blöchl, *Phys. Rev. B:Condens. Matter Mater. Phys.*, 1994, **50**, 17953.
49 J. Heyd, G. E. Scuseria and M. Ernzerhof, *J. Chem. Phys.*, 2003, **118**, 8207–8215.
50 J. Paier, M. Marsman, K. Hummer, G. Kresse, I. C. Gerber and J. G. Ángyán, *J. Chem. Phys.*, 2006, **124**, 154709.
51 A. Gali, E. Janzén, P. Deák, G. Kresse and E. Kaxiras, *Phys. Rev. Lett.*, 2009, **103**, 186404.
52 C. Freysoldt, B. Grabowski, T. Hickel, J. Neugebauer, G. Kresse, A. Janotti and C. G. Van de Walle, *Rev. Mod. Phys.*, 2014, **86**, 253–305.
53 D. Wang, L. Liu and H. L. Zhuang, *J. Appl. Phys.*, 2021, **130**, 225702.

54 B. Ramogayana, D. Santos-Carballal, K. P. Maenetja, N. H. De Leeuw and P. E. Ngoepe, *ACS Omega*, 2021, **6**, 29577–29587.
55 R. M. Hazen, *Phys. Chem. Miner.*, 1987, **14**, 13–20.
56 M. Lucht, M. Lerche, H.-C. Wille, Y. V. Shvyd'ko, H. D. Rüter, E. Gerdau and P. Becker, *J. Appl. Crystallogr.*, 2003, **36**, 1075–1081.
57 R. H. French, *J. Am. Ceram. Soc.*, 1990, **73**, 477–489.
58 V. Y. Ivanov, V. Pustovarov, E. Shlygin, A. Korotaev and A. Kruzhalov, *Phys. Solid State*, 2005, **47**, 466–473.
59 G. Thiering and A. Gali, *Phys. Rev. B*, 2017, **96**, 081115.
60 D. C. Cronemeyer, *J. Opt. Soc. Am.*, 1966, **56**, 1703.
61 H. H. Kusuma, B. Astuti and Z. Ibrahim, *J. Phys.: Conf. Ser.*, 2019, **1170**, 012054.
62 C. Song, Y. Hang, C. Xia, J. Xu and G. Zhou, *Opt. Mater.*, 2005, **27**, 699–703.
63 U. Demirbas, A. Sennaroglu and F. X. Kärtner, *Opt. Mater. Express*, 2019, **9**, 3352.
64 N. M. Trindade, A. Tabata, R. M. F. Scalvi and L. V. de Andrade Scalvi, *Mater. Sci. Appl.*, 2011, **2**, 284.
65 A. Bordage, S. Rossano, A. H. Horn and Y. Fuchs, *J. Phys.: Condens. Matter*, 2012, **24**, 225401.
66 G. Abbas, O. Bulancea-Lindvall, J. Davidsson, R. Armiento and I. A. Abrikosov, *Appl. Phys. Lett.*, 2025, **126**, 154001.
67 V. Ivády, I. A. Abrikosov, E. Janzén and A. Gali, *Phys. Rev. B:Condens. Matter Mater. Phys.*, 2013, **87**, 205201.